BurnMan – A Lower Mantle Mineral Physics Toolkit

SANNE COTTAAR

Pembroke College and University of Cambridge, Cambridge, UK

TIMO HEISTER

Clemson University, Clemson, SC, USA

IAN ROSE[*]

Earth and Planetary Science, University of California-Berkeley, Berkeley, CA 94720, USA,
ian.rose@berkeley.edu

CAYMAN UNTERBORN

The Ohio State University, Columbus, OH, USA

ABSTRACT. We present BurnMan, an open-source mineral physics toolbox to determine elastic properties for specified compositions in the lower mantle by solving an Equation of State (EoS). The toolbox, written in Python, can be used to evaluate seismic velocities of new mineral physics data or geodynamic models, and as the forward model in inversions for mantle composition. The user can define the composition from a list of minerals provided for the lower mantle or easily include their own. BurnMan provides choices in methodology, both for the EoS and for the multi-phase averaging scheme. The results can be visually or quantitatively compared to observed seismic models. Example user scripts show how to go through these steps.

This paper includes several examples realized with BurnMan: First, we benchmark the computations to check for correctness. Second, we exemplify two pitfalls in EoS modeling: using a different EoS than the one used to derive the mineral physical parameters or using an incorrect averaging scheme. Both pitfalls have led to incorrect conclusions on lower mantle composition and temperature in the literature. We further illustrate that fitting elastic velocities separately or jointly leads to different Mg/Si ratios for the lower mantle. However, we find that, within mineral physical uncertainties, a pyrolitic composition can match PREM very well. Finally, we find that uncertainties on specific input parameters result in a considerable amount of variation in both magnitude and gradient of the seismic velocities.

1. INTRODUCTION

Currently, there is no universally accepted model for the composition and temperature in Earth's lower mantle (e.g. *Cammarano et al.*, 2005; *Matas et al.*, 2007; *Cobden et al.*, 2009; *Murakami et al.*, 2012). There is considerable uncertainty in even the dominant mineralogical makeup and major element composition, i.e., the ratio of perovskite to periclase and the ratio of Mg to Si. Constraining these ratios and the temperature would go a long way in resolving several questions: are the upper and lower mantle fully mixed, or does convection mainly take place in separate layers (*Tackley*, 2000)? What is the major element bulk composition of Earth (*McDonough and Sun*, 1995)? Tomographic imaging of seismic velocities provides us with knowledge

on radial and lateral variations in velocity within Earth. However interpreting elastic properties in terms of temperature and composition requires viewing them through the lens of mineral physics (review: *Stixrude and Lithgow-Bertelloni*, 2012).

There are several reasons why no unique composition has been found. One reason is that there is no single Equation of State (EoS) to evaluate elastic properties at high pressures and temperatures – several methods are compared in *Cobden et al.* (2009). Additional non-uniqueness is inherent on the various trade-offs between the effects of composition and the choice of geotherm. Further ambiguity comes from uncertainties in mineral physical parameters for the various minerals at lower mantle conditions. Continuously improved values emerge both from experiments (e.g. *Murakami et al.*, 2012) and from first principle calculations (e.g. *Wu et al.*, 2013). Results include the effects of major element composition (e.g. *Kudo et al.*, 2012; *Noguchi et al.*, 2013), effects of the presence of volatiles (e.g. *Inoue et al.*, 2010; *Hernández et al.*, 2013) and the behavior of the spin transition in iron-bearing components (e.g. *Lin et al.*, 2007; *Antonangeli et al.*, 2011; *Mao et al.*, 2011; *Nomura et al.*, 2011; *Wu et al.*, 2013). In this study we demonstrate that part of this divergence in the interpretation is due to past studies adopting an inconsistent and incorrect methodology and from basing results on either bulk sound or shear wave velocity alone.

In this paper we present `BurnMan`, an easy-to-use, extensible, and open-source code to calculate lower-mantle seismic velocities from mineralogical models.

An important design goal for `BurnMan` is that all features should be reusable and modular, so that it is easy for the user to set up computations and plug in new minerals, averaging schemes, etc..

`Perple_X` (*Connolly*, 2005) is a powerful mineral physics code (in Fortran77) to compute phase diagrams and thermoelastic parameters allowing for a wider range of applications including phase transitions (e.g. the upper mantle and other planets). `BurnMan` is currently focused solely on the lower mantle and the comparison with seismic velocity models and does not compute phase diagrams.

While `Perple_X` is a fixed set of executables, `BurnMan` is written as a library the user interfaces from their own code. This allows incorporating novel logic and more flexible usage. Additionally, `BurnMan` is intended to be a community project under an open source licence[1] Other projects worth mentioning with some overlap with `BurnMan` include `HeFESTo`, a code in development but not available yet (L. Stixrude and others), and `Thermocalc`, a closed source, commercial project, recently extended across the mantle transition zone (*Holland et al.*, 2013).

In Section 2, we present the code structure of `BurnMan` and the reasons why `BurnMan` is written in the Python language. In Section 3.1, we discuss the various implemented methods for the mineral physical computations with and without thermal corrections. Next we cover several averaging schemes for multiphase materials (in Section 3.2.1). In Section 4, we present the various ways to define the mineral composition, choices in the geotherm, and the input of seismological models. In Section 5 we present the benchmarking and discuss examples using `BurnMan` and how the application of `BurnMan` can avoid possible pitfalls. We demonstrate the importance of consistency with regards to the choice of EoS (Section 5.2) and applying a correct averaging scheme (Section 5.3). These inconsistencies can lead to interpretations of superadiabatic temperatures, compositional gradients with depth, or a highly perovskitic lower mantle. In Section 5.4, we demonstrate fitting bulk sound and shear wave velocity independently leads to different Mg/Si ratios. However, we demonstrate that within mineral physical uncertainty the lower mantle velocities can be fit with a pyrolitic composition (Section 5.5). We end with an illustration of the effects of perturbations on mineral physical parameters (Section 5.6).

2. Toolbox Overview

The goal of `BurnMan` is to calculate seismic velocity profiles for a given mineral composition, geotherm, EoS, and averaging scheme. These calculated seismic velocity profiles can then be compared (either graphically or quantitatively) to profiles computed for other compositions or constrained by seismology. The code is available for download at `www.burnman.org`. It is written in the Python language and is run from the command line. This allows the library to be incorporated into other projects. `BurnMan` makes extensive use of SciPy and NumPy, which are widely used Python libraries for scientific computation. Matplotlib is used to display results and produce publication quality figures. The computations are consistently done in

---

[1]At the time of this writing, the source code of `Perple_X` appears to be available upon request only.

SI units, although for this paper we convert units for plotting purposes. A large collection of annotated examples on the usage of `BurnMan` are provided. Scripts to reproduce the figures in this paper are included in the toolbox. We are happy to accept contributions in form of corrections, examples, or new features.

Figure 2 shows each of the various steps in `BurnMan` and the input required at each step. The user sets the composition and temperature and pressure profiles. At later steps, the user can pick from several existing methodologies or supply an alternative implementation. This makes `BurnMan` very extensible and allows for many combinations and configurations with which to run calculations. Eventually, one can choose or provide a seismic model for comparison.

This flow setup can be used to evaluate the isotropic seismic velocities in a geodynamic model (e.g. *Davies et al.*, 2012; *Nakagawa et al.*, 2012; *Schuberth et al.*, 2012) or as the forward problem when inverting seismic profiles (e.g. *Matas et al.*, 2007; *Cobden et al.*, 2009; *Mosca et al.*, 2012) or seismic velocity variations (e.g. *Deschamps and Trampert*, 2003; *Trampert et al.*, 2004) for mineralogical compositions and temperature . The modular components of `BurnMan` can also be used separately or combined in different ways than shown in Figure 2. For example, one can input experimental results at certain pressures and temperatures and fit reference elastic moduli for a specific EoS. Additionally, one can implement their own alternatives for each of the existing modules. `BurnMan` has the potential to expand to other planetary applications. While all the features are modular, everything is available in a single library. Because of this applications consist of a single short script file (like the examples used to produce the figures in this paper) that define the setup and perform the computations, analysis, and visualization.

The current release contains the following:

- The library (in `burnman/*.py`),
- Close to 20 examples arranged as a tutorial to teach the different features of `BurnMan` (see `readme.txt` and `example_*.py`),
- A library with dozens of minerals (see `burnman/minerals/`)
- More advanced examples (including the files to generate the figures in this paper) in `misc/`.
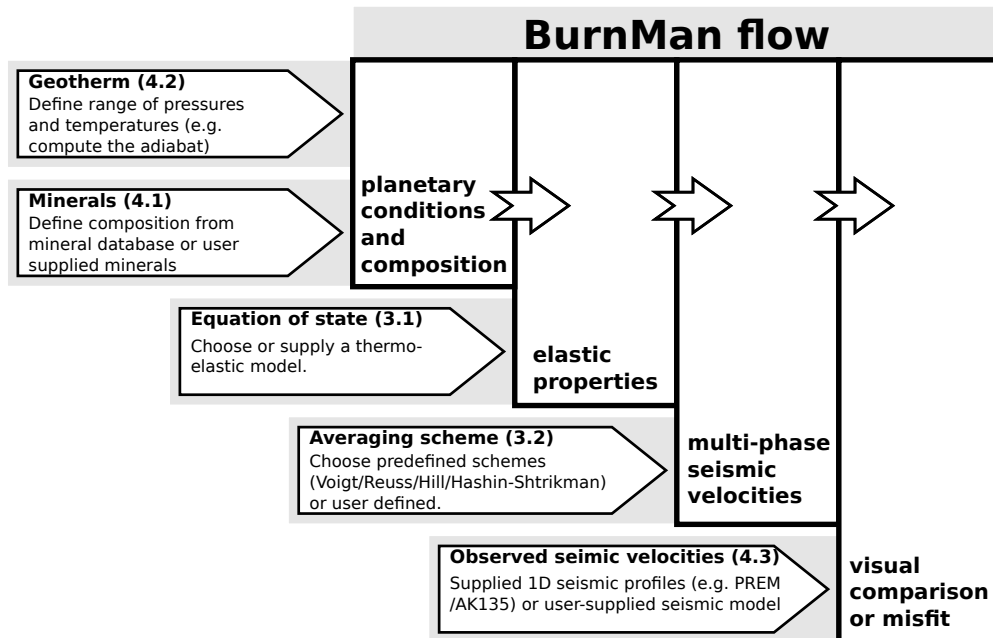
FIGURE 1. Code structure of `BurnMan`. Arrows show flow from inputs and settings into algorithms to output. The flow of a typical program is depicted by the boxes on the far left. In each stage several inputs are supplied and if predefined models are not sufficient, they can be replaced by user-written modules.

3. Methods

3.1. **Calculating Thermoelastic Properties.** To calculate the bulk (K) modulus, shear modulus (G) and density (ρ) of a material at a given pressure (P) and temperature (T, optionally defined by a geotherm) and determine the seismic velocities (V_S, V_P, V_Φ), one uses an Equation of State (EoS). Currently the following EoSs are supported in `BurnMan`: the Birch-Murnaghan formulation (excludes temperature effects) (*Poirier*, 1991), and the Birch-Murnaghan formulation with a Mie-Grüneisen-Debye temperature correction as formulated by *Stixrude and Lithgow-Bertelloni* (2005). To calculate these thermoelastic parameters, the EoS requires the user to input three parameters: pressure, temperature, the phases and their molar fractions. These inputs and outputs are further discussed in Section 4.

3.1.1. *Isothermal calculations: Birch-Murnaghan.* The Birch-Murnaghan equation is an isothermal Eulerian finite-strain EoS relating pressure and volume. The negative finite-strain (or compression) is defined as

$$(1) \qquad f = \frac{1}{2}\left[\left(\frac{V}{V_0}\right)^{-2/3} - 1\right],$$

where V is the volume at a given pressure and V_0 is the volume at a reference state ($P = 10^5$ Pa , $T = 300$ K). The pressure and elastic moduli are derived from a third order Taylor expansion of Helmholtz free energy in f and evaluating the appropriate volume and strain derivatives (see, e.g., *Poirier* (1991)). For an isotropic material one obtains for the pressure, isothermal bulk modulus, and shear modulus:

$$(2) \qquad P = 3K_0 f\left(1+2f\right)^{5/2}\left[1 + \frac{3}{2}\left(K_0' - 4\right)f\right],$$

$$(3) \qquad K_T = (1+2f)^{5/2}\left[K_0 + (3K_0 K_0' - 5K_0)f + \frac{27}{2}(K_0 K_0' - 4K_0)f^2\right],$$

$$(4) \qquad G = (1+2f)^{5/2}\left[G_0 + (3K_0 G_0' - 5G_0)f + (6K_0 G_0' - 24K_0 - 14G_0 + \frac{9}{2}K_0 K_0')f^2\right].$$

Here K_0 and G_0 are the reference bulk modulus and shear modulus and K_0' and G_0' are the derivative of the respective moduli with respect to pressure.

`BurnMan` has the option to use the second-order expansion for shear modulus by dropping the f^2 terms in these equations (as is sometimes done for experimental fits or EoS modeling). In Section 5.2 we show the importance of using a method consistent with the method used to fit the experimental result.

3.1.2. *Thermal Corrections.* Thermal corrections for pressure, and isothermal bulk modulus and shear modulus are derived from the Mie-Grüneisen-Debye EoS with the quasi-harmonic approximation. Here we adopt the formalism of *Stixrude and Lithgow-Bertelloni* (2005) where these corrections are added to equations (2)–(4):

$$(5) \qquad P_{th}(V,T) = \frac{\gamma \Delta \mathcal{U}}{V},$$

$$(6) \qquad K_{th}(V,T) = (\gamma + 1 - q)\frac{\gamma \Delta \mathcal{U}}{V} - \gamma^2 \frac{\Delta(C_V T)}{V},$$

$$(7) \qquad G_{th}(V,T) = -\frac{\eta_S \Delta \mathcal{U}}{V}.$$

The Δ refers to the difference in the relevant quantity from the reference temperature (300 K). γ is the Grüneisen parameter, q is the logarithmic volume derivative of the Grüneisen parameter, η_S is the shear strain derivative of the Grüneisen parameter, C_V is the heat capacity at constant volume, and $\mathcal{U}$ is the

internal energy at temperature T. C_V and $\mathcal{U}$ are calculated using the Debye model for vibrational energy of a lattice. These quantities are calculated as follows:

$$(8) \qquad C_V = 9nR \left(\frac{T}{\theta}\right)^3 \int_0^{\frac{\theta}{T}} \frac{e^\tau \tau^4}{(e^\tau - 1)^2} d\tau,$$

$$(9) \qquad \mathcal{U} = 9nRT \left(\frac{T}{\theta}\right)^3 \int_0^{\frac{\theta}{T}} \frac{\tau^3}{(e^\tau - 1)} d\tau,$$

$$(10) \qquad \gamma = \frac{1}{6} \frac{\nu_0^2}{\nu^2} (2f + 1) \left[a_{ii}^{(1)} + a_{iikk}^{(2)} f\right],$$

$$(11) \qquad q = \frac{1}{9\gamma} \left[18\gamma^2 - 6\gamma - \frac{1}{2}\frac{\nu_0^2}{\nu^2}(2f + 1)^2 a_{iikk}^{(2)}\right],$$

$$(12) \qquad \eta_S = -\gamma - \frac{1}{2}\frac{\nu_0^2}{\nu^2}(2f + 1)^2 a_S^{(2)},$$

$$(13) \qquad \frac{\nu^2}{\nu_0^2} = 1 + a_{ii}^{(1)} f + \frac{1}{2} a_{iikk}^{(2)} f^2,$$

$$(14) \qquad a_{ii}^{(1)} = 6\gamma_0,$$

$$(15) \qquad a_{iikk}^{(2)} = -12\gamma_0 + 36\gamma_0^2 - 18 q_0 \gamma_0,$$

$$(16) \qquad a_S^{(2)} = -2\gamma_0 - 2\eta_{S0},$$

where θ is the Debye temperature of the mineral, ν is the frequency of vibrational modes for the mineral, n is the number of atoms per formula unit (e.g. 2 for periclase, 5 for perovskite), and R is the gas constant. Under the approximation that the vibrational frequencies behave the same under strain, we may identify $\nu/\nu_0 = \theta/\theta_0$. The quantities γ_0, η_{S0} q_0, and θ_0 are the experimentally determined values for those parameters at the reference state.

Due to the fact that a planetary mantle is rarely isothermal along a geotherm, It is more appropriate to use the adiabatic bulk modulus K_S instead of K_T, which is calculated using

$$(17) \qquad K_S = K_T(1 + \gamma\alpha T),$$

where α is the coefficient of thermal expansion

$$(18) \qquad \alpha = \frac{\gamma C_V V}{K_T}.$$

There is no difference between the isothermal and adiabatic shear moduli for an isotropic solid. All together this makes an eleven parameter EoS model, which is summarized in Table 1. For more details on the EoS, we refer readers to *Stixrude and Lithgow-Bertelloni* (2005).

3.2. Calculating multi-phase seismic velocities.

3.2.1. *Averaging schemes.* After the thermoelastic parameters (K_S, G, ρ) of each phase are determined at each pressure and/or temperature step, these values must be combined to determine the seismic velocity of a multiphase assemblage. We define the volume fraction of the individual minerals in an assemblage:

$$(19) \qquad \nu_i = n_i \frac{V_i}{V},$$

where V_i and n_i are the molar volume and the molar fractions of the ith individual phase, and V is the total molar volume of the assemblage:

$$(20) \qquad V = \sum_i n_i V_i.$$

The density of the multiphase assemblage is then

$$(21) \qquad \rho = \sum_i \nu_i \rho_i = \frac{1}{V} \sum_i n_i \mu_i,$$

where ρ_i is the density and μ_i is the molar mass of the ith phase.

TABLE 1. Overview of mineral physical user inputs. Note that all units throughout the code are in SI.

User Input	Symbol	Definition	Units
V_0	V_0	Volume at P $= 10^5$ Pa , T $= 300$ K	m^3 mol^{-1}
K_0	K_0	Isothermal bulk modulus at $P = 10^5$ Pa, T $= 300$ K	Pa
Kprime_0	K_0'	Pressure derivative of K_0	-
G_0	G_0	Shear modulus at P $= 10^5$ Pa, T $= 300$ K	Pa
Gprime_0	G_0'	Pressure derivative of G_0	-
molar_mass	μ	mass per mole formula unit	kg mol^{-1}
n	n	number of atoms per formula unit	-
Debye_0	θ_0	Debye Temperature	K
grueneisen_0	γ_0	Grüneisen parameter at P $= 10^5$ Pa, T $= 300$ K	-
q0	q_0	Logarithmic volume derivative of the Grüneisen parameter	-
eta_s_0	η_{S0}	Shear strain derivative of the Grüneisen parameter	-

Unlike density and volume, there is no straightforward way to average the bulk and shear moduli of a multiphase rock, as it depends on the specific distribution and orientation of the constituent minerals. BurnMan allows several schemes for averaging the elastic moduli: the Voigt and Reuss bounds, the Hashin-Shtrikman bounds, the Voigt-Reuss-Hill average, and the Hashin-Shtrikman average (*Watt et al.*, 1976).

The Voigt average, assuming constant strain across all phases, is defined as

$$(22) \qquad X_V = \sum_i \nu_i X_i,$$

where X_i is the bulk or shear modulus for the ith phase. The Reuss average, assuming constant stress across all phases, is defined as

$$(23) \qquad X_R = \left(\sum_i \frac{\nu_i}{X_i} \right)^{-1}.$$

The Voigt-Reuss-Hill average is the arithmetic mean of Voigt and Reuss bounds:

$$(24) \qquad X_{VRH} = \frac{1}{2} \left(X_V + X_R \right).$$

The Hashin-Shtrikman bounds make an additional assumption that the distribution of the phases is statistically isotropic, and are usually much narrower than the Voigt and Reuss bounds (*Watt et al.*, 1976). This may be a poor assumption in regions of Earth with high anisotropy, such as the lowermost mantle, though they are rather more physically motivated than the commonly-used Voigt-Reuss-Hill average. In most instances, the Voigt-Reuss-Hill average and the arithmetic mean of the Hashin-Shtrikman bounds are quite close to each other with the pure arithmetic mean (linear averaging) being well outside of both Hashin-Shtrikman and Voigt-Reuss-Hill (Figure 2).

It is worth noting that each of the above bounding methods are derived from mechanical models of a linear elastic composite. It is thus only appropriate to apply them to elastic moduli, and not to other thermoelastic properties, such as wave speeds or density.

3.2.2. *Computing seismic velocities.* Once the moduli for the multiphase assemblage are computed, the compressional (P), shear (S) and bulk sound (Φ) velocities are then result from the equations:

$$(25) \qquad V_P = \sqrt{\frac{K_S + \frac{4}{3}G}{\rho}}, \qquad V_S = \sqrt{\frac{G}{\rho}}, \qquad V_\Phi = \sqrt{\frac{K_S}{\rho}}.$$
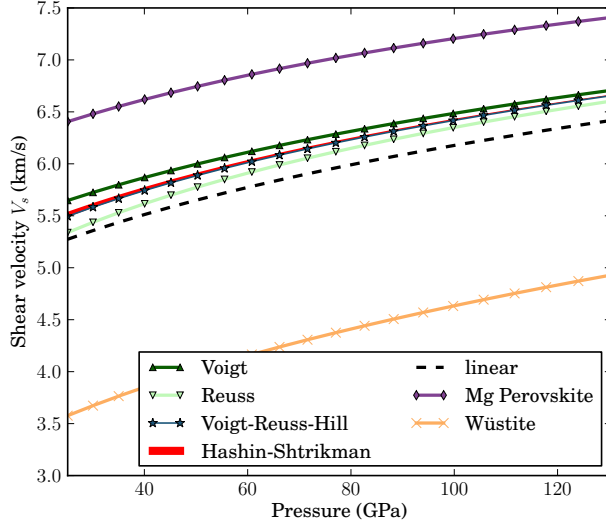
FIGURE 2. Illustration of different averaging schemes with a rock made from 60% perovskite and 40% wüstite calculated using the 3rd order formulation of equation (3) and (4) with thermal corrections. Voigt, Reuss, Voigt-Reuss-Hill, and Hashin-Shtrikman averages are shown as a function of pressure. For reference, the two end members are also shown. The geotherm used is *Brown and Shankland* (1981) and the EoS parameters are from *Stixrude and Lithgow-Bertelloni* (2011). This figure can be reproduced with `misc/paper_averaging.py`.

To correctly compare to observed seismic velocities one needs to correct for the frequency sensitivity of attenuation. Moduli parameters are obtained from experiments that are done at high frequencies (MHz-GHz) compared to seismic frequencies (mHz-Hz). The frequency sensitivity of attenuation causes slightly lower velocities for seismic waves than they would be for high frequency waves. In `BurnMan` one can correct the calculated acoustic velocity values to those for long period seismic tomography (*Minster and Anderson*, 1981):

$$(26) \qquad V_{S/P} = V_{S/P}^{\text{uncorr.}} \left(1 - \frac{1}{2} \cot(\frac{\beta\pi}{2}) \frac{1}{Q_{S/P}}(\omega) \right).$$

Similar to *Matas et al.* (2007), we use a β value of 0.3, which falls in the range of values of 0.2 to 0.4 proposed for the lower mantle (e.g. *Karato and Spetzler* (1990)). The correction is implemented for Q values of PREM for the lower mantle. As Q_S is smaller than Q_P, the correction is more significant for S waves. In both cases, though, the correction is minor compared to, for example, uncertainties in the temperature (corrections) and mineral physical parameters. More involved models of relaxation mechanisms can be implemented, but lead to the inclusion of more poorly constrained parameters, (*Matas and Bukowinski*, 2007). While attenuation can be ignored in many applications (*Trampert et al.*, 2001), it might play a significant role in explaining strong variations in seismic velocities in the lowermost mantle (*Davies et al.*, 2012).

4. User input

4.1. **Mineralogical composition.** A number of pre-defined minerals are included in the mineral library and users can create their own. The library includes wrapper functions to include a transition from the high-spin mineral to the low-spin mineral (review: *Lin et al.*, 2013) or to combine minerals for a given iron number.

Standard minerals – The 'standard' mineral format includes a list of parameters given in Table 1. Each mineral includes a suggested EoS with which the mineral parameters are derived. For some minerals the parameters for the thermal corrections are not yet measured or calculated, and therefore the corrections can

not be applied. An occasional mineral will not have a measured or calculated shear moduli, and therefore can only be used to compute densities and bulk sound velocities. The mineral library is subdivided by citation. BurnMan includes the option to produce a LaTeX table of the mineral parameters used. BurnMan can be easily setup to incorporate uncertainties for these parameters.

Minerals with a spin transition – A standard mineral for the high spin and low spin must be defined separately. These minerals are "wrapped," so as to switch from the high spin to high spin mineral at a give pressure. While not realistic, for the sake of simplicity, the spin transitions are considered to be sharp at a given pressure.

Minerals depending on Fe partitioning – The wrapper function can partition iron, for example between ferropericlase, fp, and perovskite, pv. It requires the input of the iron mol fraction with regards to Mg, X_{fp} and X_{pv}, which then defines the chemistry of an Mg-Fe solid solution according to $(\text{Mg}_{1-X_{\text{Fe}}^{\text{fp}}}, \text{Fe}_{X_{\text{Fe}}^{\text{fp}}})\text{O}$ or $(\text{Mg}_{1-X_{\text{Fe}}^{\text{pv}}}, \text{Fe}_{X_{\text{Fe}}^{\text{pv}}})\text{SiO}_3$. The iron mol fractions can be set to be constant or varying with P and T as needed. Alternatively one can calculate the iron mol fraction from the distribution coefficient K_D defined as

$$(27) \qquad K_D = \frac{X_{\text{Fe}}^{\text{pv}}/X_{\text{Mg}}^{\text{pv}}}{X_{\text{Fe}}^{\text{fp}}/X_{\text{Mg}}^{\text{fp}}}.$$

We adopt the formalism of *Nakajima et al.* (2012) choosing a reference distribution coefficient K_{D0} and standard state volume change (Δv^0) for the Fe-Mg exchange between perovskite and ferropericlase

$$(28) \qquad K_D = K_{D0} \exp\left(\frac{(P_0 - P)\Delta v^0}{RT}\right),$$

where R is the gas constant and P_0 the reference pressure. As a default, we adopt the average Δv^0 of *Nakajima et al.* (2012) of $2 \cdot 10^{-7}$ m^3 mol^{-1} and suggest using their K_{D0} value of 0.5.

The multiphase mixture of these minerals can be built by the user in three ways:

(1) Molar fractions of an arbitrary number of pre-defined minerals, for example mixing standard minerals mg_perovskite (MgSiO$_3$), fe_perovskite (FeSiO$_3$), periclase (MgO) and wüstite (FeO).

(2) A two-phase mixture with constant or (P, T) varying Fe partitioning using the minerals that include Fe-dependency, for example mixing $(\text{Mg}, \text{Fe})\text{SiO}_3$ and $(\text{Mg}, \text{Fe})\text{O}$ with a pre-defined distribution coefficient.

(3) Weight percents (wt%) of (Mg, Si, Fe) and distribution coefficient (includes (P,T)-dependent Fe partitioning). This calculation assumes that each element is completely oxidized into its corresponding oxide mineral (MgO, FeO, SiO$_2$) and then combined to form iron-bearing perovskite and ferropericlase taking into account some Fe partition coefficient.

4.2. **Geotherm.** Unlike the pressure, the temperature of the lower mantle is relatively unconstrained. As elsewhere, BurnMan provides a number of built-in geotherms, as well as the ability to use user-defined temperature-depth relationships. A geotherm in BurnMan is an object that returns temperature as a function of pressure. Alternatively, the user could ignore the geothermal and compute elastic velocities for a range of temperatures at any give pressure.

Currently, we include geotherms published by *Brown and Shankland* (1981) and *Anderson* (1982). Alternatively one can use an adiabatic gradient defined by the thermoelastic properties of a given mineralogical model. For a homogeneous material, the adiabatic temperature profile is given by integrating the ordinary differential equation (ODE)

$$(29) \qquad \left(\frac{\mathrm{d}T}{\mathrm{d}P}\right)_S = \frac{\gamma T}{K_S}.$$

This equation can be extended to multiphase composite using the first law of thermodynamics to arrive at

$$(30) \qquad \left(\frac{\mathrm{d}T}{\mathrm{d}P}\right)_S = \frac{T \sum_i \dfrac{n_i C_{Pi} \gamma_i}{K_{Si}}}{\sum_i n_i C_{Pi}},$$

where the subscripts correspond to the ith phase, C_P is the heat capacity at constant pressure of a phase, and the other symbols are as defined above. Integrating this ODE requires a choice in anchor temperature (T_0) at the top of the lower mantle (or including this as a parameter in an inversion). As the adiabatic geotherm is dependent on the thermoelastic parameters at high pressures and temperatures, it is dependent on the equation of state used.

4.3. **Seismic Models.** `BurnMan` allows for direct visual and quantitative comparison with seismic velocity models. Various ways of plotting can be found in the examples. Quantitative misfits between two profiles include an L2-norm and a chi-squared misfit, but user defined norms can be implemented. A seismic model in `BurnMan` is an object that provides pressure, density, and seismic velocities (V_P, V_Φ, V_S) as a function of depth.

To compare to seismically constrained profiles, `BurnMan` provides the 1D seismic velocity model PREM (*Dziewonski and Anderson*, 1981). One can choose to evaluate $V_P, V_\Phi, V_S, \rho, K_S$ and/or G. The user can input their own seismic profile, an example of which is included for AK135 (*Kennett et al.*, 1995).

Besides standardized 1D radial profiles, one can also compare to regionalized average profiles for the lower mantle. This option accommodates the observation that the lowermost mantle can be clustered into two regions, a 'slow' region, which represents the so-called Large Low Shear Velocity Provinces, and 'fast' region, the continuous surrounding region where slabs might subduct (*Lekic et al.*, 2012). This clustering as well as the averaging of the 1D model occurs over five tomographic S wave velocity models (SAW24B16: (*Mégnin and Romanowicz*, 2000); HMSL-S: (*Houser et al.*, 2008); S362ANI: (*Kustowski et al.*, 2008); GyPSuM: (*Simmons et al.*, 2010); S40RTS: (*Ritsema et al.*, 2011)). The strongest deviations from PREM occur in the lowermost 1000 km. Using the 'fast' and 'slow' S wave velocity profiles is therefore most important when interpreting the lowermost mantle. Suggestion of compositional variation between these regions comes from seismology (e.g. *To et al.*, 2005; *He and Wen*, 2012) as well as geochemistry (e.g. *Deschamps et al.*, 2012; *Jackson et al.*, 2010) Based on thermo-chemical convection models, *Styles et al.* (2011) also show that averaging profiles in thermal boundary layers may cause problems for seismic interpretation .

We additionally apply cluster analysis to and provide models for P wave velocity based on two tomographic models (MIT-P08: (*Li and van der Hilst*, 2008); GyPSuM: (*Simmons et al.*, 2012)). The clustering results correlate well with the fast and slow regions for S wave velocities; this could well be due to the fact that the initial model for the P wave velocity models is scaled from S wave tomographic velocity models. Additionally, the variations in P wave velocities are a lot smaller than for S waves. For this reason using these adapted models is most important when comparing the S wave velocities.

While interpreting lateral variations of seismic velocity in terms of composition and temperature is a major goal (*Trampert et al.*, 2004; *Mosca et al.*, 2012), to determine the bulk composition the current challenge appears to be concurrently fitting absolute P and S wave velocities (Section 5.4) and incorporate the significant uncertainties in mineral physical parameters (Section 5.6).

5. RESULTS

5.1. **Benchmarking.** `BurnMan` consists of many modules, and every attempt is made to benchmark them for correctness, both individually as well as together. Additionally, we include a set of unit tests to ensure that changes and additions to the code do not break existing functionality. Figure 3 shows a comparison with the output of the mantle thermodynamics code `HeFESTo` [*L. Stixrude*, personal communication, 2013] for forsterite at zero pressure over a range of temperatures. In all cases the error is less than $5 \cdot 10^{-4}\%$.

5.2. **Extrapolating shear moduli.** The Birch-Murnaghan EoS is based on a Taylor expansion. Therefore, it is incorrect to fit parameters to one order of an EoS and applying these in an extrapolation with a different order. For example, fitting data to a 2nd order EoS and applying these calculated parameters to a 3rd order EoS extrapolation will produce a slower shear velocity than that of the 2nd order extrapolation at each pressure.

Figure 4 illustrates the error introduced when using inconsistent orders of the EoS. We fit measurements of V_S from *Murakami et al.* (2012) to 2nd and 3rd order Birch-Murnaghan EoS using least squares. The bulk properties are set to the values listed in Table 5.2 and calculated using equations (1)–(4). The values fitted by different orders vary by 2.5% in G_0 and 10% in G_0'. Using 2nd order values in a 3rd order extrapolation will underestimate the velocities, while 3rd order values in a 2nd order extrapolation result in higher velocities
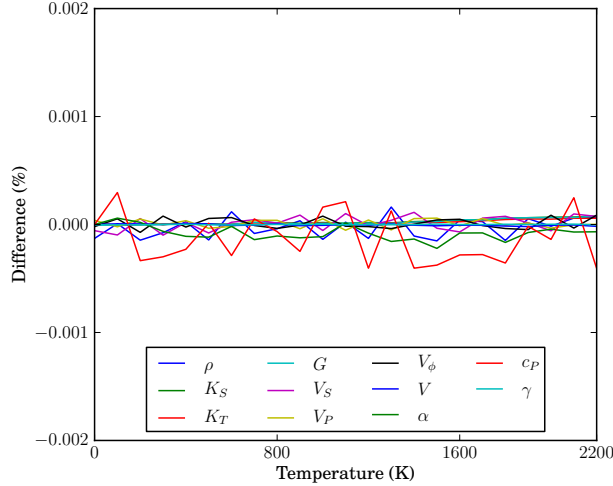
FIGURE 3. Comparison of calculated thermodynamic and elastic parameters for forsterite from `BurnMan` with those computed from the code `HeFESTo` [*L. Stixrude*, personal communication, 2013] at zero pressure and a range of temperatures. This figure can be reproduced with `misc/paper_benchmark.py`.
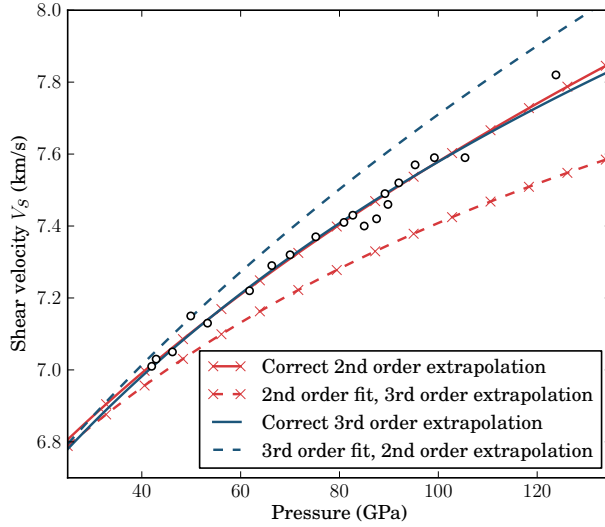
FIGURE 4. V_S measurements fitted with the 2nd (red) and 3rd (blue) order EoS. Dashed lines illustrate the error that results from extrapolating shear wave velocities with the incorrect order. Measurements (open circles) are for Mg-perovskite with 4wt% Al_2O_3 from *Murakami et al.* (2012). This figure can be reproduced with `misc/paper_fit_data.py`.

(dashed lines). The latter leads to interpreting superadiabatic temperatures or a compositional gradient with depth (*Matas et al.*, 2007). The deviations in velocity increase up to 5% at the highest pressures. In this example the experimental data lie in the lower mantle pressure range, but the discrepancy would be higher if we only had measurements in the lower pressure ranges.

The bulk modulus, however, is less sensitive when applying an inconsistent order when extrapolating than the shear modulus. This is due to the 3rd order term in the calculation of bulk modulus being small because K_0' is often about 4.

TABLE 2. Parameters used to fit V_S measurements of Mg-perovskite with 4wt% Al_2O_3 from *Murakami et al.* (2012). The first four parameters are used in the fit of the data and are values for pure Mg-perovskite (*Stixrude and Lithgow-Bertelloni*, 2005). The next four values are the resulting G_0 and G'_0 produced by the fit of a given order.

Parameter	Value
V_0	$24.45 \cdot 10^{-6}$ m^3/mol
K_0	281 GPa
K'_0	4.1
molar mass	0.10227 kg/mol
G_0 2nd order	173.3 GPa
G'_0 2nd order	1.52
G_0 3rd order	168.9 GPa
G'_0 3rd order	1.67

Besides applying inconsistent orders, incorrect results can occur when combining G_0 and G'_0 from different experimental data sources as the two values are linked. Additionally, when temperature is considered, the thermal corrections need to be handled in the same way. `BurnMan` provides the tools to fit the mineral physical data (`example_fit_data.py`) and apply them with consistent methods. Its mineral library contains the suggested EoS to use for each mineral defined.

5.3. **Significance of the averaging scheme.** Here we show that incorrect averaging leads to interpreting a strongly perovskitic mantle, i.e., an Mg/Si ratio close to 1. We compute seismic velocities using the same mineral physical parameters as *Murakami* (2013) (table 6.3, and references therein). The values for G'_0 from *Murakami et al.* (2007, 2009) are roughly 0.2 lower than other published values (for example (*Stixrude and Lithgow-Bertelloni*, 2011)). The lower values are fit using the second order EoS, relating to the issue illustrated in Section 5.2. The author shows that higher G'_0 values would lead to anomalously high velocities, which can lead to incorrect interpretations in general due to using a 2nd order EoS with values derived for the 3rd order EoS (Section 5.2) . For consistency, we use the published G'_0 values of *Murakami* (2013) with a second order EoS and the geotherm from *Brown and Shankland* (1981) .

While our single phase computations agree well with *Murakami* (2013), our results diverge when averaging the two phases to an aggregate velocity. The left panel of Figure 5 shows the computations adopting a Voigt-Reuss-Hill averaging scheme on the elastic moduli (Section 3.2.1). The best fitting model with this averaging scheme is 83% perovskite. However, the best fit as found by *Murakami* (2013) of 92% perovskite results in shear velocities that are too fast. In the right panel of Figure 5, we attempt to fit the velocities as computed by *Murakami* (2013) with an incorrect averaging scheme. Here we average the velocities by their phase fractions (instead of moduli using volume fractions):

$$(31) \qquad V_S = \frac{1}{2}\left(\sum_i n_i V_{Si} + \left(\sum_i \frac{n_i}{V_{Si}}\right)^{-1}\right).$$

With this averaging method, PREM is best fit by 92% perovskite and the results (visually) match.

These computations invalidate previous claims of a highly perovskitic lower mantle. We find that a closer-to-pyrolitic composition fits the shear wave velocities in PREM. In the next example, however, we will demonstrate that fitting shear wave velocities alone is not sufficient.

5.4. **Jointly fitting bulk sound and shear velocities.** In Figure 6 we show an example of a parameter search for the amount of perovskite for a homogeneous lower mantle. We minimize the L^2 norm between the computations and observed seismic velocities. For this case we use the recent mineral data from *Stixrude and Lithgow-Bertelloni* (2011) and *Zhang et al.* (2013) (see Table 5.4); we mix perovskite with 7% Fe and ferropericlase with 20% Fe. We use the EoS (to third order) and thermal corrections as formulated in *Stixrude and Lithgow-Bertelloni* (2005) (see Section 3.1). The geotherm is an adiabatic temperature profile

TABLE 3. Parameters from *Stixrude and Lithgow-Bertelloni* (2011) and *Zhang et al.* (2013) used in Sections 5.4 and 5.5. The published uncertainties on G_0' for the perovskite phases of zero have been modified to 0.1 (italic). The "Used" columns refer to the values used in Figure 7 where we deviate from the literature values.

Parameter	Mg-Perovskite		Used	Fe-Perovskite		Used	Periclase		Used	Wüstite		Used
V_0 (m^3/mol)	2.445e-5			2.549e-5			1.124e-5			1.226e-5		
K_0 (Pa)	250.5e9	(3e9)		272e9	(40e9)	263.7e9	161e9	(3e9)		179e9	(1e9)	
K_0'	4.01	(0.1)	3.917	4.1	(1.0)	3.428	3.8	(0.2)	3.718	4.9	(0.2)	
G_0 (Pa)	172.9e9	(2e9)		133e9	(40e9)		131e9	(1e9)		59e9	(1e9)	
G_0'	1.74	*(0.1)*	1.779	1.4	*(0.1)*		2.1	(0.1)		1.4	(0.1)	
molar mass (kg/mol)	0.1			0.1319			0.0403			0.0718		
n	5			5			2			2		
$\theta_0(K)$	905.9	(5)		871	(26)		767	(9)		454	(21)	
γ_0	1.44	(0.05)		1.57	(0.3)		1.36	(0.05)		1.53	(0.13)	
q_0	1.09	(0.3)		1.1	(1.0)		1.7	(0.2)		1.7	1.0)	
η_{S0}	2.13	(0.3)		2.3	(1.0)		2.8	(0.2)		-0.1	(1.0)	

with an anchor temperature of 1900 K at the top of the lower mantle (see Section 4.2). We also adopt a Voigt-Reuss-Hill averaging scheme.

Figure 6 shows that V_Φ and V_S can be fit up to an acceptable error at the same time, whereas fitting only one of the velocities (especially V_S) would argue for a 10% difference in perovskite content. Regardless of the choice of optimum mixture, V_Φ and V_S differ by roughly one percent relative to PREM. Additionally, above ∼80 GPa, V_Φ and V_S diverge from each other relative to PREM. This parameter search demonstrates that it is insufficient to fit only V_Φ or V_S with a simple model to constrain composition. This parameter set does a relatively good job, as also argued by *Zhang et al.* (2013), while other parameter sets we've tried– for
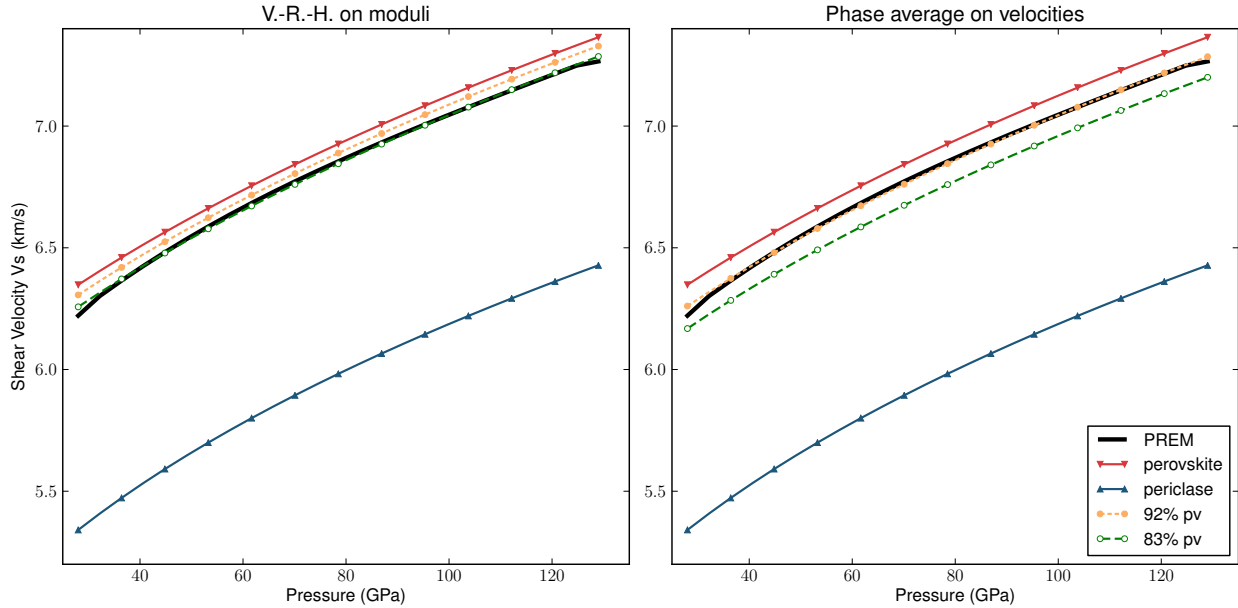
FIGURE 5. V_S computations for pure perovskite, periclase, mixtures of 92% perovskite with 8% periclase, and 83% perovskite with 17% periclase for two different averaging schemes. In the first panel, the two phases are averaged by the Voigt-Reuss-Hill scheme resulting in a best fit of 83% perovskite. In the second panel, velocities represent a phase fraction weighted average of velocities and slownesses, which results in previously published best fits of 92% perovskite. This figure can be reproduced with `misc/example_incorrect_averaging.py`.
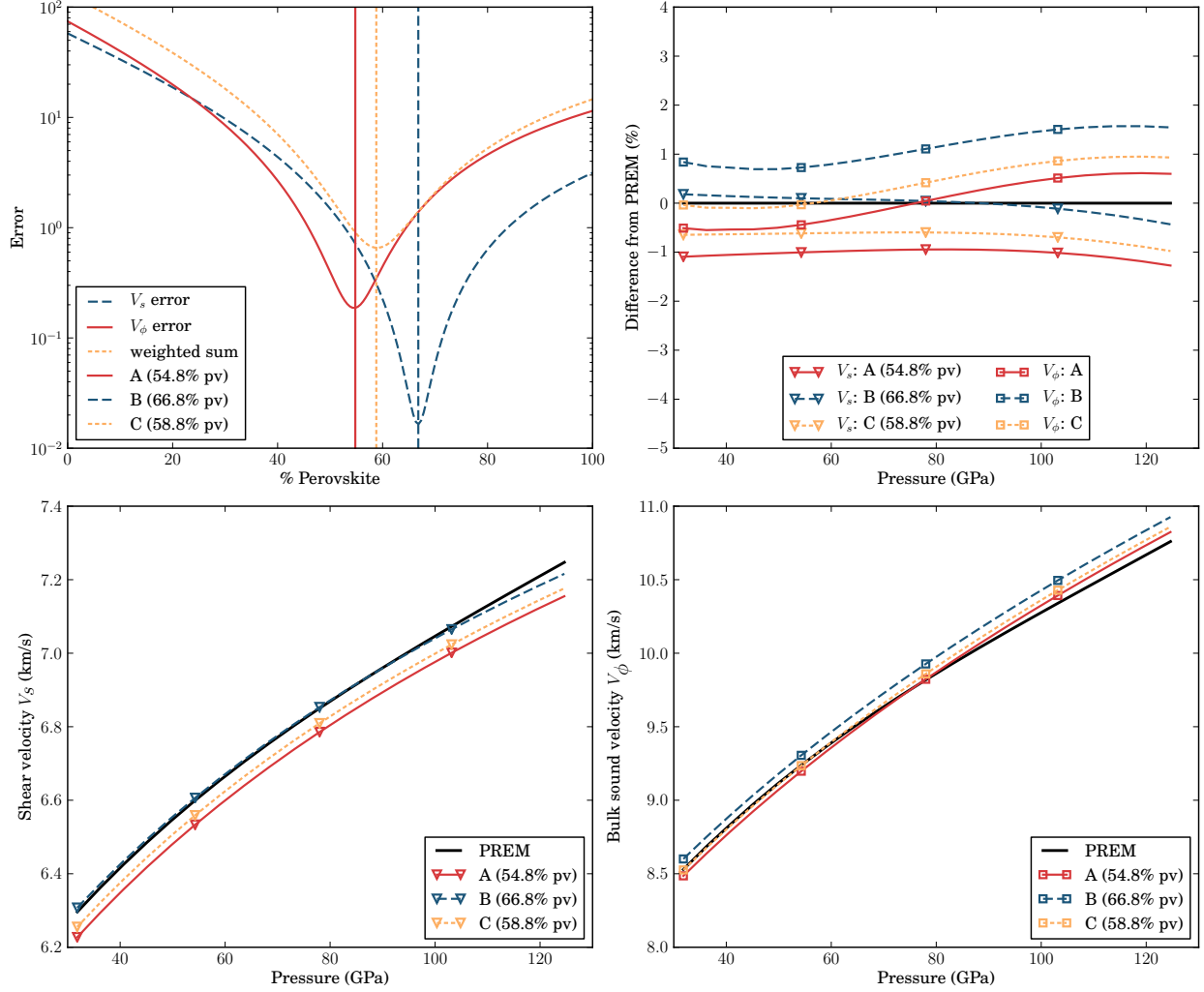
FIGURE 6. Given end member minerals of perovskite (7% Fe) and ferropericlase (20% Fe), the optimum molar percentage of perovskite necessary to fit PREM is determined by minimizing the L^2 norm of the error in both V_Φ (red, solid) and V_S (blue, dashed) independently (upper left). Minimizing V_Φ finds a best fit of 54.8% perovskite (Mixture A, red, solid), while minimizing V_S finds 66.8% perovskite as the best fit (Mixture B, blue, long-dashed). Both L^2 norms are weighted by their respective average PREM velocities and then added to give the weighted error (yellow, short-dashed). The combined norm finds 58.8% perovskite (Mixture C, yellow, short-dashed). Percent differences between PREM and V_Φ (squares) or V_S (triangles) for each of the mixtures are shown in the upper right figure. Final velocity profiles are shown in the bottom row. For these calculations we adopt the input parameters of *Stixrude and Lithgow-Bertelloni* (2011) and *Zhang et al.* (2013) listed in Table 5.4. This figure can be reproduced with `misc/paper_opt_pv.py`.

example the set for the previous examples– show a difference in the amount of perovskite of 25% to 30%. Solely fitting V_Φ (e.g. *Ita and Stixrude*, 1992; *Mattern et al.*, 2005) always leads to a larger Mg/Si ratio than solely fitting V_S (e.g. *Murakami et al.*, 2012). The discrepancies between fitting both velocities remain when changing the iron content or the anchor temperature of the adiabat.

Choosing to fit V_P would essentially be fitting a weighted average between V_Φ and V_S (see equations 25). However, solely fitting V_P, without concurrently fitting V_S and ρ, could result in fitting correct velocities for
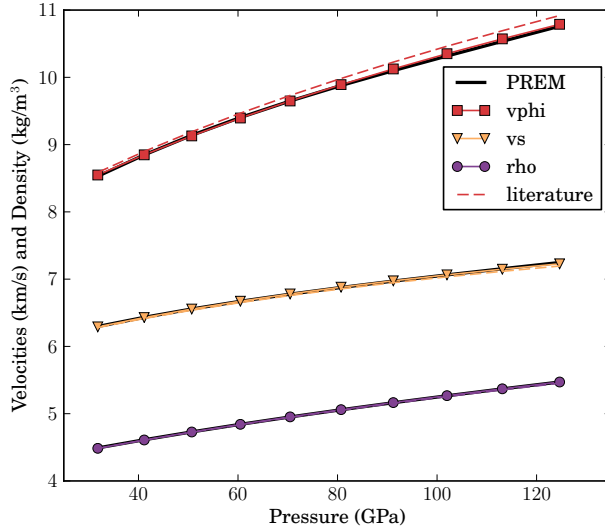
FIGURE 7. Seismic velocities and density for a simplified pyrolitic composition with published reference values (dashed) and fitted values within uncertainty bounds (solid) compared to PREM (black). We adopt a pyrolite composition of 67% perovskite (with 7% Fe) and 33 % periclase (with 20% Fe). The parameters and uncertainties are from *Stixrude and Lithgow-Bertelloni* (2011) and *Zhang et al.* (2013) (Table 5.4). This figure can be reproduced with `misc/paper_onefit.py`.

the wrong reasons, i.e., the computed μ and K_S are separately not consistent with what is observed in the Earth.

5.5. **Fitting PREM within mineral physical uncertainties.** The next two examples illustrate the capabilities for including uncertainties on mineral physical parameters in `BurnMan`. When including published uncertainties on mineral physical parameters, one can find a good fit to seismic velocities and density for a chosen composition. We choose a simplified pyrolitic composition consisting of 67% perovskite and 33% periclase: including Fe in both phases and ignoring the effects of Al and Ca. We use the 3rd order EoS with an adiabatic temperature profile and average the elastic moduli using the arithmetic mean of the Hashin-Shtrikman bounds.

We use the same data set from Table 5.4, but allow for perturbations on the parameters within uncertainty as well as variation on the anchor temperature. We search through the parameter space by computing random perturbations on the parameters and eventually choose a good solution that has a small number of values where we deviate from the literature values. The perturbed values (shown in separate columns in Table 5.4) and an anchor temperature of 2000 K at a depth of 850km lead to an extremely good fit of PREM in Figure 7. It is important to note that these values do not represent a unique solution, but rather an example solution. Additionally, fitting PREM velocities and density with such precision might be over-interpreting the accuracy of the seismic constraints and the averaging scheme.

5.6. **Propagating uncertainty.** The EoS applied here has a large number of parameters, many of which are poorly constrained for important mantle minerals. It it not always obvious from the EoS what effect a parameter has on the calculated seismic wave velocities. We have performed an uncertainty propagation for V_Φ and V_S of Mg-perovskite by varying eight parameters (Table 1). As we are interested in the sensitivities to uncertainty in the parameters, we do not attempt to use realistic estimates of uncertainty here, but instead use values of 50% for γ_0, q_0, and η_{S0}, and 10% for all other values. We calculate the wave velocities from 850-2700 km depth along an adiabat with an anchor temperature (T_0) of 1900 K±10%. The results of this analysis are shown in Figure 8.

As one might expect from the form of the equations, V_Φ is insensitive to G_0, G_0', and η_{S0}. Furthermore, as all calculations are well above the Debye temperature, there is little sensitivity to θ_0. Less obvious is the
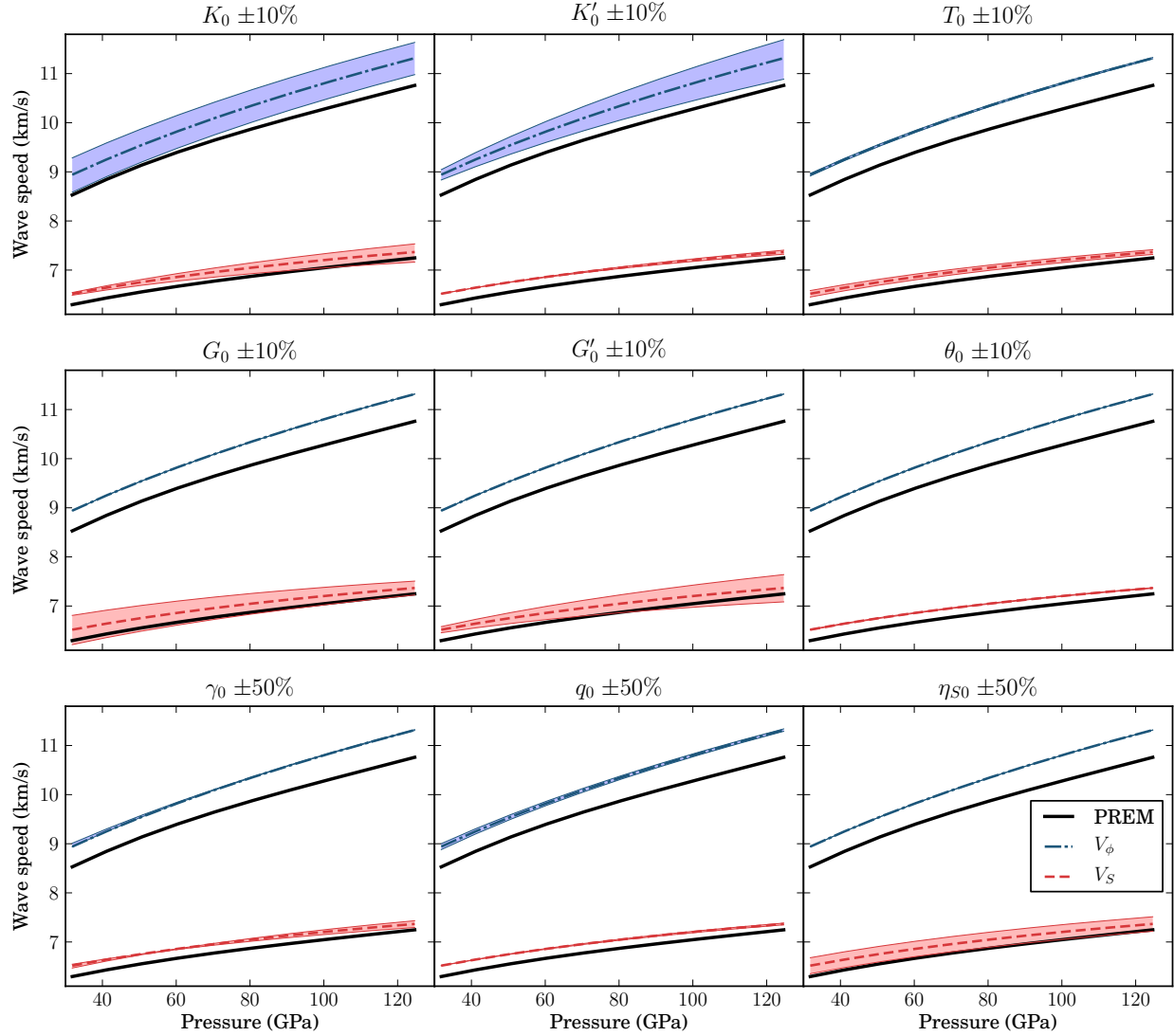
FIGURE 8. The effects of varying mineral physical parameters and anchor temperature of the adiabatic for V_Φ (blue) and V_S (red). Reference values are from *Stixrude and Lithgow-Bertelloni* (2011). The parameters γ_0, q_0, and η_{S0} are varied by $\pm 50\%$ while all other parameters mentioned are varied by $\pm 10\%$. In each image only one parameter is varied and all others are held at the reference values. This figure can be reproduced with `misc/paper_uncertain.py`.

small (especially for V_Φ) effect of varying the other parameters for the thermal corrections (γ_0, q_0, and η_{S0}) even when changing them by $\pm 50\%$.

In general, the wave velocities are most sensitive to the parameters controlling the isothermal contributions to the elastic moduli; the same parameters that required perturbation in Section 5.5. These examples illustrate that uncertainties need to be published (e.g *Stixrude and Lithgow-Bertelloni*, 2011) and incorporated in analyses as new results emerge (e.g. *Trampert et al.*, 2004; *Cammarano et al.*, 2005; *Cobden et al.*, 2009). While experimental uncertainties remain large, they contribute to the non-uniqueness of the solution and complicate the interpretation of lateral variations in seismic velocities.

6. Conclusions

We present an easily scriptable, open-source, multidisciplinary toolbox for the lower mantle. `BurnMan` can compute seismic velocities for a composite of minerals at high pressures and temperatures, or be used to fit the elastic moduli from experimental or seismic observations. Applying `BurnMan`, we illustrate the importance of using an EoS that is consistent with that used for fitting experimental data and adopting the correct averaging scheme. Previous incorrect computations in the literature have led to interpretations of an overly perovskitic lower mantle, super adiabatic temperatures, or compositional variations with depth. We illustrate that fitting solely bulk sound velocity or shear wave velocity can lead to variation in amount of perovskite in the lower mantle. Incorporating published uncertainties on mineral physical parameters can lead to an excellent, yet non-unique, fit for a pyrolitic composition. We find that uncertainties in the elastic moduli have a significant effect on the seismic velocities and should be incorporated into every analysis.

We hope to have convinced the reader that:

(1) The correct and consistent computation of seismic properties from mineral properties is difficult.
(2) There is a need for a consistent framework to calculate these velocity profiles so as to confidently compare results from different sources.
(3) The usage of a tool like `BurnMan` gives you the confidence that the computations are correct (due to extensive testing and benchmarking).
(4) `BurnMan` is easy to use and tests can be developed quickly: initial versions of all of the examples were created in a few hours. The logic is typically contained in only a few lines of code.
(5) Flexibility is important. The ability to compare different methods (and plugging in your own) gives important insights.

Finally, we hope that the development and release of `BurnMan` enables the community to do exciting research.

7. Acknowledgments

References

Anderson, O. L. (1982), The earth's core and the phase diagram of iron, *Philos. T. Roy. Soc. A*, *306*(1492), 21–35.

Antonangeli, D., J. Siebert, C. Aracne, D. Farber, A. Bosak, M. Hoesch, M. Krisch, F. Ryerson, G. Fiquet, and J. Badro (2011), Spin crossover in ferropericlase at high pressure: a seismologically transparent transition?, *Science*, *331*(6031), 64–67.

Brown, J., and T. Shankland (1981), Thermodynamic parameters in the Earth as determined from seismic profiles, *Geophys. J. Int.*, *66*(3), 579–596.

Cammarano, F., S. Goes, A. Deuss, and D. Giardini (2005), Is a pyrolitic adiabatic mantle compatible with seismic data?, *Earth Planet. Sci. Lett.*, *232*(3), 227–243.

Cobden, L., S. Goes, M. Ravenna, E. Styles, F. Cammarano, K. Gallagher, and J. Connolly (2009), Thermo-chemical interpretation of 1-D seismic data for the lower mantle: The significance of nonadiabatic thermal gradients and compositional heterogeneity, *J. Geophys. Res.*, *114*, B11,309.

Connolly, J. (2005), Computation of phase equilibria by linear programming: a tool for geodynamic modeling and its application to subduction zone decarbonation, *Earth Planet. Sci. Lett.*, *236*(1), 524–541.

Davies, D., S. Goes, J. Davies, B. Shuberth, H.-P. Bunge, and J. Ritsema (2012), Reconciling dynamic and seismic models of Earth's lower mantle: The dominant role of thermal heterogeneity, *Earth Planet. Sci. Lett.*, *353*, 253–269.

Deschamps, F., and J. Trampert (2003), Mantle tomography and its relation to temperature and composition, *Phys. Earth Planet. Int.*, *140*(4), 277–291, doi:10.1016/j.pepi.2003.09.004.

Deschamps, F., L. Cobden, and P. Tackley (2012), The primitive nature of large low shear-wave velocity provinces, *Earth Planet. Sci. Lett.*, *349-350*, 198–208.

Dziewonski, A. M., and D. L. Anderson (1981), Preliminary reference Earth model, *Phys. Earth Planet. Int.*, *25*(4), 297–356.

He, Y., and L. Wen (2012), Geographic boundary of the Pacific Anomaly and its geometry and transitional structure in the north, *J. Geophys. Res.-Sol. Ea.*, *117*(B9), doi:DOI:10.1029/2012JB009436.

Hernández, E., D. Alfè, and J. Brodholt (2013), The incorporation of water into lower-mantle perovskites: A first-principles study, *Earth Planet. Sci. Lett.*, *364*, 37–43.

Holland, T. J. B., N. F. C. Hudson, R. Powell, and B. Harte (2013), New Thermodynamic Models and Calculated Phase Equilibria in NCFMAS for Basic and Ultrabasic Compositions through the Transition Zone into the Uppermost Lower Mantle, *Journal of Petrology*, *54*(9), 1901–1920, doi:10.1093/petrology/egt035.

Houser, C., G. Masters, P. Shearer, and G. Laske (2008), Shear and compressional velocity models of the mantle from cluster analysis of long-period waveforms, *Geophys. J. Int.*, *174*(1), 195–212.

Inoue, T., T. Wada, R. Sasaki, and H. Yurimoto (2010), Water partitioning in the Earth's mantle, *Phys. Earth Planet. Int.*, *183*(1), 245–251.

Ita, J., and L. Stixrude (1992), Petrology, elasticity, and composition of the mantle transition zone, *Journal of Geophysical Research*, *97*(B5), 6849, doi:10.1029/92JB00068.

Jackson, M. G., R. W. Carlson, M. D. Kurz, P. D. Kempton, D. Francis, and J. Blusztajn (2010), Evidence for the survival of the oldest terrestrial mantle reservoir, *Nature*, *466*(7308), 853–856.

Karato, S., and H. Spetzler (1990), Defect microdynamics in minerals and solidstate mechanisms of seismic wave attenuation and velocity dispersion in the mantle, *Rev. Geophys.*, *28*(4), 399–421.

Kennett, B., E. R. Engdahl, and R. Buland (1995), Constraints on seismic velocities in the Earth from traveltimes, *Geophys. J. Int.*, *122*(1), 108–124.

Kudo, Y., K. Hirose, M. Murakami, Y. Asahara, H. Ozawa, Y. Ohishi, and N. Hirao (2012), Sound velocity measurements of $CaSiO_3$ perovskite to 133 GPa and implications for lowermost mantle seismic anomalies, *Earth Planet. Sci. Lett.*, *349*, 1–7.

Kustowski, B., G. Ekström, and A. Dziewoski (2008), Anisotropic shear-wave velocity structure of the Earth's mantle: a global model, *J. Geophys. Res.*, *113*(B6), B06,306.

Lekic, V., S. Cottaar, A. M. Dziewonski, and B. Romanowicz (2012), Cluster analysis of global lower mantle tomography: A new class of structure and implications for chemical heterogeneity, *Earth Planet. Sci. Lett.*, *357-358*, 68–77.

Li, C., and R. van der Hilst (2008), A new global model for P wave speed variations in Earth's mantle, *Geochem. Geophys. Geosyst.*, *9*(5).

Lin, J., S. Speziale, Z. Mao, and H. Marquardt (2013), Effects of the electronic spin transitions of iron in lower mantle minerals: Implications for deep mantle geophysics and geochemistry, *Rev. Geophys.*, *Rev. Geoph*(early view).

Lin, J.-F., G. Vank, S. D. Jacobsen, V. Iota, V. V. Struzhkin, V. B. Prakapenka, A. Kuznetsov, and C.-S. Yoo (2007), Spin transition zone in Earth's lower mantle, *Science*, *317*(5845), 1740–1743.

Mao, Z., J. Lin, H. Scott, H. Watson, V. Prakapenka, Y. Xiao, P. Chow, and C. McCammon (2011), Iron-rich perovskite in the Earth's lower mantle, *Earth Planet. Sci. Lett.*, *309*(3), 179–184.

Matas, J., and M. Bukowinski (2007), On the anelastic contribution to the temperature dezpendence of lower mantle seismic velocities, *Earth Planet. Sci. Lett.*, *259*(1), 51–65.

Matas, J., J. Bass, Y. Ricard, E. Mattern, and M. Bukowinski (2007), On the bulk composition of the lower mantle: predictions and limitations from generalized inversion of radial seismic profiles, *Geophys. J. Int.*, *170*(2), 764–780.

Mattern, E., J. Matas, Y. Ricard, and J. Bass (2005), Lower mantle composition and temperature from mineral physics and thermodynamic modelling, *Geophys. J. Int.*, *160*(3), 973–990, doi:10.1111/j.1365-246X.

2004.02549.x.

McDonough, W., and S. Sun (1995), The composition of the Earth, *Chem. Geol.*, *120*(3), 223–253.

Mégnin, C., and B. Romanowicz (2000), The three-dimensional shear velocity structure of the mantle from the inversion of body, surface and higher-mode waveforms, *Geophys. J. Int.*, *143*(3), 709–728.

Minster, J., and D. Anderson (1981), A model of dislocation-controlled rheology for the mantle, *Phil. Trans. R. Soc. Lond.*, *299*(1449), 319–359.

Mosca, I., L. Cobden, A. Deuss, J. Ritsema, and J. Trampert (2012), Seismic and mineralogical structures of the lower mantle from probabilistic tomography, *J. Geophys. Res.: Solid Earth*, *117*(B6).

Murakami, M. (2013), 6 Chemical Composition of the Earth's Lower Mantle: Constraints from Elasticity, in *Physics and Chemistry of the Deep Earth (ed S.-I. Karato)*, pp. 183–212, John Wiley & Sons, Ltd, Chichester, UK.

Murakami, M., S. Sinogeikin, H. Hellwig, J. Bass, and J. Li (2007), Sound velocity of MgSiO3 perovskite to Mbar pressure, *Earth Planet. Sci. Lett.*, *256*(1-2), 47–54, doi:10.1016/j.epsl.2007.01.011.

Murakami, M., Y. Ohishi, N. Hirao, and K. Hirose (2009), Elasticity of MgO to 130 GPa: Implications for lower mantle mineralogy, *Earth Planet. Sci. Lett.*, *277*(1-2), 123–129, doi:10.1016/j.epsl.2008.10.010.

Murakami, M., Y. Ohishi, N. Hirao, and K. Hirose (2012), A perovskitic lower mantle inferred from high-pressure, high-temperature sound velocity data., *Nature*, *485*(7396), 90–94.

Nakagawa, T., P. Tackley, F. Deschamps, and J. Connolly (2012), Radial 1D seismic structures in the deep mantle in mantle convection simulations with selfconsistently calculated mineralogy, *Geochem. Geophys. Geosyst.*, *13*(11).

Nakajima, Y., D. Frost, and D. Rubie (2012), Ferrous iron partitioning between magnesium silicate perovskite and ferropericlase and the composition of perovskite in the Earth's lower mantle, *J. Geophys. Res.*, *117*(B8).

Noguchi, M., T. Komabayashi, K. Hirose, and Y. Ohishi (2013), High-temperature compression experiments of CaSiO_3 perovskite to lowermost mantle conditions and its thermal equation of state, *Phys. Chem. Miner.*, *40*(1), 81–91.

Nomura, R., H. Ozawa, S. Tateno, K. Hirose, J. Hernlund, S. Muto, H. Ishii, and N. Hiraoka (2011), Spin crossover and iron-rich silicate melt in the Earth's deep mantle, *Nature*, *473*(7346), 199–202.

Poirier, J. (1991), *Introduction to the Physics of the Earth*, Cambridge Univ. Press, Cambridge, England.

Ritsema, J., A. Deuss, H. J. van Heijst, and J. Woodhouse (2011), S40RTS: a degree-40 shear-velocity model for the mantle from new Rayleigh wave dispersion, teleseismic traveltime and normal-mode splitting function, *Geophys. J. Int.*, *184*(3), 1223–1236.

Schuberth, B., C. Zaroli, and G. Nolet (2012), Synthetic seismograms for a synthetic Earth: long-period P- and S-wave traveltime variations can be explained by temperature alone, *Geophys. J. Int.*, *188*(3), 1393–1412.

Simmons, N., A. Forte, L. Boschi, and S. Grand (2010), GyPSuM: A joint tomographic model of mantle density and seismic wave speeds, *J. Geophys. Res.*, *115*(B12), B12,310.

Simmons, N., S. Myers, G. Johanneson, and E. Matzel (2012), LLNLG3Dv3: Global P wave tomography model for improved regional and teleseismic travel time prediction, *J. Geophys. Res.*, *117*(B10).

Stixrude, L., and C. Lithgow-Bertelloni (2005), Thermodynamics of mantle mineralsI. Physical properties, *Geophys. J. Int.*, *162*(2), 610–632.

Stixrude, L., and C. Lithgow-Bertelloni (2011), Thermodynamics of mantle mineralsII. Phase equilibria, *Geophys. J. Int.*, *184*(3), 1180–1213.

Stixrude, L., and C. Lithgow-Bertelloni (2012), Geophysics of chemical heterogeneity in the mantle, *Annu. Rev. Earth Planet. Sci.*, *40*, 569–595.

Styles, E., D. R. Davies, and S. Goes (2011), Mapping spherical seismic into physical structure: biases from 3-D phase-transition and thermal boundary-layer heterogeneity, *Geophys. J. Int.*, *184*(3), 1371–1378, doi:10.1111/j.1365-246X.2010.04914.x.

Tackley, P. (2000), Mantle convection and plate tectonics: Toward an integrated physical and chemical theory, *Science*, *288*(5473), 2002–2007.

To, A., B. Romanowicz, Y. Capdeville, and N. Takeuchi (2005), 3D effects of sharp boundaries at the borders of the African and Pacific Superplumes: Observation and modeling, *Earth Planet. Sci. Lett.*, *233*(1-2), 1447–1460.

Trampert, J., P. Vacher, and N. Vlaar (2001), Sensitivities of seismic velocities to temperature, pressure and composition in the lower mantle, *Phys. Earth Planet. Int.*, *124*(3-4), 255–267, doi:10.1016/S0031-9201(01)00201-1.

Trampert, J., F. Deschamps, J. Resovsky, and D. Yuen (2004), Probabilistic tomography maps chemical heterogeneities throughout the lower mantle., *Science (New York, N.Y.)*, *306*(5697), 853–6, doi:10.1126/science.1101996.

Watt, J., G. Davies, and R. O'Connell (1976), The elastic properties of composite materials, *Rev. Geophys.*, *14*(4), 541–563.

Wu, Z., J. Justo, and R. Wentzcovitch (2013), Elastic Anomalies in a Spin-Crossover System: Ferropericlase at Lower Mantle Conditions, *Phys. Rev. Lett.*, *110*(22), 228,501.

Zhang, Z., L. Stixrude, and J. Brodholt (2013), Elastic properties of MgSiO3-perovskite under lower mantle conditions and the composition of the deep Earth, *Earth Planet. Sci. Lett.*, *379*, 1–12, doi:10.1016/j.epsl.2013.07.034.